



City Research Online

City, University of London Institutional Repository

Citation: Odry, B., Kiraly, A. P., Slabaugh, G. G., Novak, C. L., Naidich, D. L. & Lerallut, J. (2008). Active contour approach for accurate quantitative airway analysis. Progress in Biomedical Optics and Imaging - Proceedings of SPIE, 6916, 691613. doi: 10.1117/12.772592

This is the accepted version of the paper.

This version of the publication may differ from the final published version.

Permanent repository link: <https://openaccess.city.ac.uk/id/eprint/4388/>

Link to published version: <https://doi.org/10.1117/12.772592>

Copyright: City Research Online aims to make research outputs of City, University of London available to a wider audience. Copyright and Moral Rights remain with the author(s) and/or copyright holders. URLs from City Research Online may be freely distributed and linked to.

Reuse: Copies of full items can be used for personal research or study, educational, or not-for-profit purposes without prior permission or charge. Provided that the authors, title and full bibliographic details are credited, a hyperlink and/or URL is given for the original metadata page and the content is not changed in any way.

Active contour approach for accurate quantitative airway analysis

Benjamin L. Odry^a, Atilla P. Kiraly^a, Greg G. Slabaugh^a, Carol L. Novak^a, David P. Naidich^b and Jean-Francois Lerallut^c

^aSiemens Corporate Research, Inc, Princeton NJ USA 08540;

^bDept. of Radiology, New York University Medical Center, New York, NY USA 10016

^cUMR CNRS Heudiasyc, Université de Technologie de Compiègne, Compiègne France 60201

ABSTRACT

Chronic airway disease causes structural changes in the lungs including peribronchial thickening and airway dilatation. Multi-detector computed tomography (CT) yields detailed near-isotropic images of the lungs, and thus the potential to obtain quantitative measurements of lumen diameter and airway wall thickness. Such measurements would allow standardized assessment, and physicians to diagnose and locate airway abnormalities, adapt treatment, and monitor progress over time. However, due to the sheer number of airways per patient, systematic analysis is infeasible in routine clinical practice without automation. We have developed an automated and real-time method based on active contours to estimate both airway lumen and wall dimensions; the method does not require manual contour initialization but only a starting point on the targeted airway. While the lumen contour segmentation is purely region-based, the estimation of the outer diameter considers the inner wall segmentation as well as local intensity variation, in order to anticipate the presence of nearby arteries and exclude them. These properties make the method more robust than the Full-Width Half Maximum (FWHM) approach. Results are demonstrated on a phantom dataset with known dimensions and on a human dataset where the automated measurements are compared against two human operators. The average error on the phantom measurements was 0.10mm and 0.14mm for inner and outer diameters, showing sub-voxel accuracy. Similarly, the mean variation from the average manual measurement was 0.14mm and 0.18mm for inner and outer diameters respectively.

Keywords: airway measurements, active contour

1. INTRODUCTION

CT evaluation of airway abnormalities is problematic without standardized methods for assessing location and severity. Additionally, inter- and intra-observer variability limits both diagnostic sensitivity and reliable evaluation of response to therapy from follow-up CT. Automated airway quantification is therefore a necessity for a systematic analysis of the bronchial tree. The major challenge for airway measurement techniques resides in the accuracy and reproducibility, in order to allow comparison of pre and post intervention and thus evaluation of therapeutic response. Measurements of small structures in CT images are subject to distortions caused by partial volume effect and the point spread function of the scanner.

Several approaches have been explored to quantify the airway, but none have become a gold standard yet. Thanks to the quasi isotropic nature of datasets from MDCT, most techniques are able to evaluate 2D cross-sections perpendicular to the airway's principal axes to assess dimensions.

The Full Width Half Maximum (FWHM) principle was one of the first methods developed to measure airway dimensions and has been frequently used as a point of comparison. It determines the location of the lumen as half way in between the maximum and minimum gray levels [1]. It creates an under-estimation of inner diameter and over-estimation of outer diameters. Some newer techniques based on the FWHM principle involve the inclusion of the segmentation data [2], or use of radial derivatives to perform unsupervised computation [3], and show improvements in measurement accuracy and robustness.

Another approach uses the 2D or 3D point spread function (PSF) of the CT scanner to provide accurate measurements of the airways. A cylinder is used to fit the shape of the airway and an estimated PSF is used [4]. However, the PSF estimation is sensitive to noise and therefore to the acquisition protocol of the image. Also, the method is based on assuming a cylindrical model for the airway, which is not always an accurate assumption.

A priori knowledge methods have also been developed, relying on characteristic properties of the bronchi that can be modeled in image analysis [5, 6]. One method combines morphological filtering, connection-cost based marking and conditional watershed techniques. Calibration was realized on phantom datasets and validated by expert radiologists' evaluations. More recently, radially re-sampled cross sections have been used for the airway inner measurements [7]. The lumen is resampled into a linear structure and the inner diameter is estimated using dynamic programming a cost function is based on a calibrated balance between first and second derivatives. Kiraly *et al* introduced targeted cost functions for both inner and outer diameters coupled with additional costs to exclude adjacent vessels from the segmentation [8].

Interestingly, most of those methods utilize gradient information to proceed with their evaluation. To the best of our knowledge, an active contour approach, which also generally uses a gradient map and initial contour to perform general segmentation, has never previously been applied to airway measurements until now. Besides the use of gradient maps, active contour approaches also offer region-based segmentation to separate regions with weak boundaries. This is especially applicable to small airways where the walls are often affected by partial volume.

2. METHODOLOGY

2.1. Background on active contours

The basic idea in active contour models or snakes is to evolve a curve based on specific constraints, in order to extract meaningful features from an image. Usually, a curve is initialized around the outside of the object to be detected, and moves inward to stop at the boundary of the object. Classical snakes and active contour models use a gradient-based edge-detector to halt the evolving curve on the boundaries of the object. The model usually has three terms, two to control the smoothness of the contour (internal energy) and a third one to control the attraction to the object (external energy).

More rigorously, Ω is a bounded open subset of \mathbb{R}^2 , with $\partial\Omega$ as its boundary, representing the active curve and its internal contents. Let $I: \overline{\Omega} \rightarrow \mathbb{R}$ be a given image and $C(s): [0,1] \rightarrow \mathbb{R}^2$ a parameterized curve. The snake model is $\inf_C J_1(C)$ where:

$$J_1(C) = \alpha \int_0^1 |C'(s)|^2 ds + \beta \int_0^1 |C''(s)| ds - \lambda \int_0^1 |\nabla I(C(s))|^2 ds \quad (1)$$

By minimizing this energy, the curve locates the maxima of $|\nabla I|$ acting as an edge-detector. A general detector is usually defined by a positive and decreasing function g that depends on the gradient of the image I such as $\lim_{x \rightarrow \infty} g(x) = 0$.

The edge detector can be expressed as follows:

$$g(|\nabla I(x, y)|) = \frac{1}{1 + |\nabla G_0(x, y) * I(x, y)|^p}, \quad p \geq 1 \quad (2)$$

where $G_0 * I$, a smoother version of I , is the convolution between I and the Gaussian $G_0(x, y) = \sigma^{-2} e^{-|x^2 + y^2|/2\sigma^2}$. $g(|\nabla I(x, y)|)$ is zero at the edges and positive in homogeneous regions. The curve C is represented implicitly by a Lipschitz function $\phi: C = \{(x, y) | \phi(x, y) = 0\}$ and the curve evolution is given by the zero-level curve at time t of $\phi(t, x, y)$. The evolution of the curve is realized in the normal direction with speed F and can be expressed as:

$$\frac{\partial \phi}{\partial t} = |\nabla \phi| F, \quad \phi(0, x, y) = \phi_0(x, y) \quad (3)$$

For a geometric active contour model based on the mean curvature motion, the evolution equation is the following:

$\frac{\partial \phi}{\partial t} = g(|\nabla I|) \nabla \phi (k + \nu)$ with $k = \text{div} \left(\frac{\nabla \phi(x, y)}{|\nabla \phi(x, y)|} \right)$, as the curvature of the level-curve of ϕ passing through (x, y) , or

Euclidian curvature, and ν is a positive constant. This process of geodesic active contour model has been thoroughly detailed in [9].

An extension of the work on active contours is described in [10], focusing on the intensity of the object to segment rather than the gradient of the image. It allows the algorithm to segment objects with weak boundaries, where the gradient would not be usable. Chan proposes a model without an edge-based gradient function to stop the process.

Following the same notations, C denotes the boundary of w , an open subset of Ω , $\text{Inside}(C)$ denotes this region w and $\text{outside}(C)$ denotes the region $\Omega \setminus w$. The idea is that, assuming the image contains two distinct objects of piecewise-constant intensities, I_i and I_o , with I_i being the intensity value of the targeted object and I_o the value outside this object, there exists an optimum curve C_0 such as $\text{inside}(C_0) = I_i$ and $\text{outside}(C_0) = I_o$. This fitting term can be expressed as follow:

$$F_1(C) + F_2(C) = \int_{\text{inside}(C)} |I(x, y) - \mu_{in}|^2 dx dy + \int_{\text{outside}(C)} |I(x, y) - \mu_{out}|^2 dx dy \quad (4)$$

where C is a variable curve and μ_{in} , μ_{out} are the averages of I inside C and outside C respectively. C_0 is the boundary that satisfies the minimization of $F_1(C) + F_2(C)$. Consequently, the functional energy to minimize is:

$$\begin{aligned} F(\mu_{in}, \mu_{out}, C) = & \alpha \cdot \text{Length}(C) + \beta \cdot \text{Area}(\text{inside}(C)) \\ & + \lambda_1 \int_{\text{inside}(C)} |I(x, y) - \mu_{in}|^2 dx dy \\ & + \lambda_2 \int_{\text{outside}(C)} |I(x, y) - \mu_{out}|^2 dx dy \end{aligned} \quad (5)$$

where the length of the curve and/or the area of the region inside C are regularizing parameters and $\alpha \geq 0, \beta \geq 0, \lambda_1, \lambda_2 > 0$ are fixed parameters. Using the Heaviside function H and the one dimensional Dirac measure δ_0 defined as:

$$H(z) = \begin{cases} 1, & \text{if } z \geq 0 \\ 0, & \text{if } z < 0 \end{cases} \quad \delta_0(z) = \frac{d}{dz} H(z) \quad (6)$$

The functional energy can then be rewritten as:

$$\begin{aligned} F(\mu_{in}, \mu_{out}, \phi) = & \alpha \cdot \int_{\Omega} \delta(\phi(x, y)) |\nabla \phi(x, y)| dx dy \\ & + \beta \cdot \int_{\Omega} H(\phi(x, y)) dx dy \\ & + \lambda_1 \int_{\Omega} |I(x, y) - \mu_{in}|^2 H(\phi(x, y)) dx dy \\ & + \lambda_2 \int_{\Omega} |I(x, y) - \mu_{out}|^2 (1 - H(\phi(x, y))) dx dy \end{aligned} \quad (7)$$

where the first term expresses the contour length, the second term the area within the contour.

Ultimately, the speed term characterizing the descent direction can be expressed as:

$$\frac{\partial \phi}{\partial t} = \delta(\phi) \left[\alpha \cdot \text{div} \left(\frac{\nabla \phi}{|\nabla \phi|} \right) - \beta - \lambda_1 (I - \mu_{in})^2 + \lambda_2 (I - \mu_{out})^2 \right] \quad (8)$$

with $\text{div}\left(\frac{\nabla\phi(x,y)}{|\nabla\phi(x,y)|}\right)$ the Euclidian curvature at $\phi(x,y)$.

Using these formulations of active contour models, we can define the regions we need to segment and the correct functional energy to minimize.

2.2. Method

The measurement process uses a 2D cross-section perpendicular to the principle axes of the bronchus at the selected location. The airway orientation is provided by the previously processed tracheobronchial hierarchical tree [11, 12]. In case this information is not available, the orientation can be determined locally as explained in [13, 14]. Our approach uses an unraveled image that we compute using a radial transformation of the trilinear interpolated perpendicular cross section of the airway, starting from the airway center. The inner / outer boundary segmentation therefore should ideally correspond to a line. It becomes easier to deal with partial volume effect and prevent leakage into the parenchyma. The airway segmentation is done in two steps, one for the inner wall boundary and one for the outer wall. The outer wall estimation depends on the final inner boundary segmentation.



Figure 1: Perpendicular cross-section to the airway principle axes and corresponding unraveled image. The lumen area is shown at the bottom of the unraveled image.

2.2.1. Inner wall estimation

We define an initial contour C as a horizontal line across the luminal area. Here, to simplify the process, we consider C as a polygon instead of the implicit active contour. The number of points of the polygon is stable during the curve evolution process since it depends on the resolution of the unraveled image. Each point p_i on the polygon is issued from ray i at angle θ_i with a radius $r(\theta_i)$ from the image center. The connection of all the neighboring points represents the polygon. Each polygon point is expressed as:

$$p_i = \begin{bmatrix} \theta_i \\ r(\theta_i) \end{bmatrix} \quad (9)$$

The inner wall estimation consists of finding a partial differential equation (PDE) that updates $r(\theta_i)$ such that the energy is minimized.

Since the luminal area has a uniform intensity corresponding to the density of air, we choose to use a region-based segmentation to separate it from the rest of the image. To preserve the circularity of the boundary, we also add a smoothness constraint between the points along the curve.

The active contour energy equation that we are going to use can be expressed as follows:

$$E(C) = \lambda_1 \int_{\Omega_{in}} (I(x, y) - \mu_{in})^2 d\Omega_{in} + \lambda_2 \int_{\Omega_{out}} (I(x, y) - \mu_{out})^2 d\Omega_{out} + \alpha \cdot Length(C) \quad (10)$$

Here, the area term is not utilized. The length of the curvature is expressed through the curvature on the speed term definition. More specifically in our case, the speed term $\frac{\partial r}{\partial t} = F \cdot N$ with F as the force term that deforms the contour and N as the normal at polygon p_i .

$$\frac{\partial r}{\partial t} = \left(\lambda_1 (I(p_i) - \mu_{in})^2 - \lambda_2 (I(p_i) - \mu_{out})^2 + \alpha \cdot K \right) \cdot N \bullet \begin{bmatrix} 0 \\ 1 \end{bmatrix} \quad (11)$$

where $I(p_i)$ is the value of the image at p_i . μ_{in} and μ_{out} are the means inside and outside the contour, or here the regions below and above the contour. K is the curvature of the curve at p_i , N is the curve normal at p_i , α is a term that weights the curvature term relative to the data term, and λ_1, λ_2 are fixed parameters. The update vector is oriented along the curve normal. The last dot product \bullet projects it onto the y axis of the transformed image along which $r(\theta_i)$ is evolved.

Since the image is unraveled, the curvature is computed using both ends of the image to simulate the closed contour.



Figure 2. Initial active contour



Figure 3. Contour evolution at intermediate step, i=20 iterations

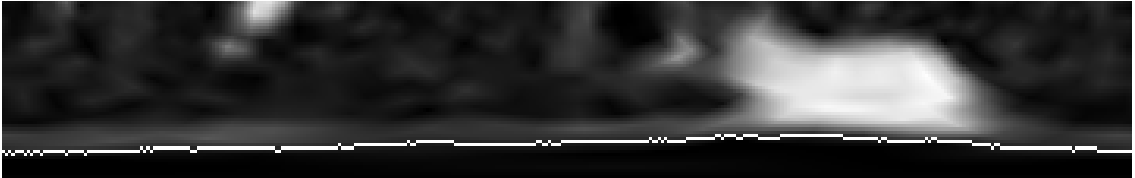


Figure 4. Contour evolution at final step, i=63 iterations

2.2.2. Outer wall estimation

Now that the inner boundary is segmented, we use it to set an initial contour to segment the outer wall of the airway. For every polygon point of the inner contour, we increase the radius by 4 pixels on the image to set the initial outer contour, $C_{out}(0)$. It is not possible, however, to apply the exact same approach as for the inner wall. The density of the wall is less uniform than that of the lumen. Moreover, in the presence of an adjacent artery with much higher intensity, the region-based active contour would include the vessel as a part of the wall (see Figures 5 and 6).

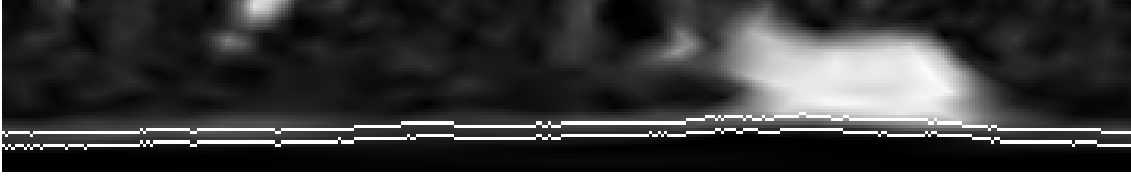


Figure 5: Outer wall initialization as an offset of the inner wall estimation.

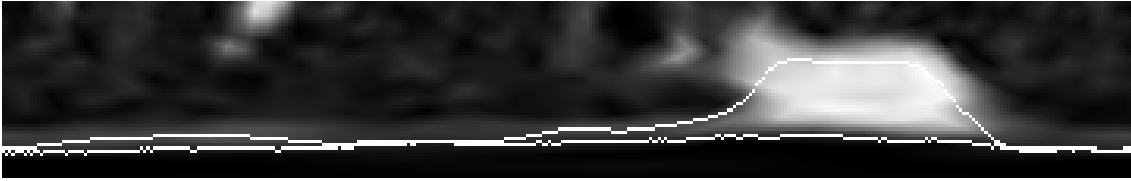


Figure 6: Active contour using the region-based approach after 90 iterations. The vessel is included in the outer wall segmentation. Intensity difference therefore causes outer wall to cross the inner wall.

We therefore take a more local approach. We define a distance d_i between the p_{out_i} and p_i . Using the region-based active contour approach, we separate the mean along the ray within the distance d_i before and after p_{out_i} . At each evolution step, d_i will be updated and the speed term accordingly. Again, to link the polygon points and ensure a smoothness of the contour, we use a curvature constraint as shown previously for the inner wall estimation.

The speed term becomes:

$$\frac{\partial r}{\partial t} = \left(\lambda_1 \left(I(p_{out_i}) - v_{in}(d_i) \right)^2 - \lambda_2 \left(I(p_{out_i}) - v_{out}(d_i) \right)^2 + \alpha \cdot K \right) \cdot N \cdot \begin{bmatrix} 0 \\ 1 \end{bmatrix} \quad (13)$$

where $v_{in}(d_i)$ and $v_{out}(d_i)$ respectively represent the mean of the pixels along a length d_i of the ray i from p_{out_i} respectively towards the inside and outside regions (below / above).

The result of the segmentation after 999 iterations using this speed term is shown in Figure 8. The local region-based segmentation using the distance allows for a good separation of the wall from the rest of the image. Problems occur around the artery where the mean separation causes both under and over segmentation. The curvature constraint does not help smooth out the curve in this case as it does without the presence of an artery.

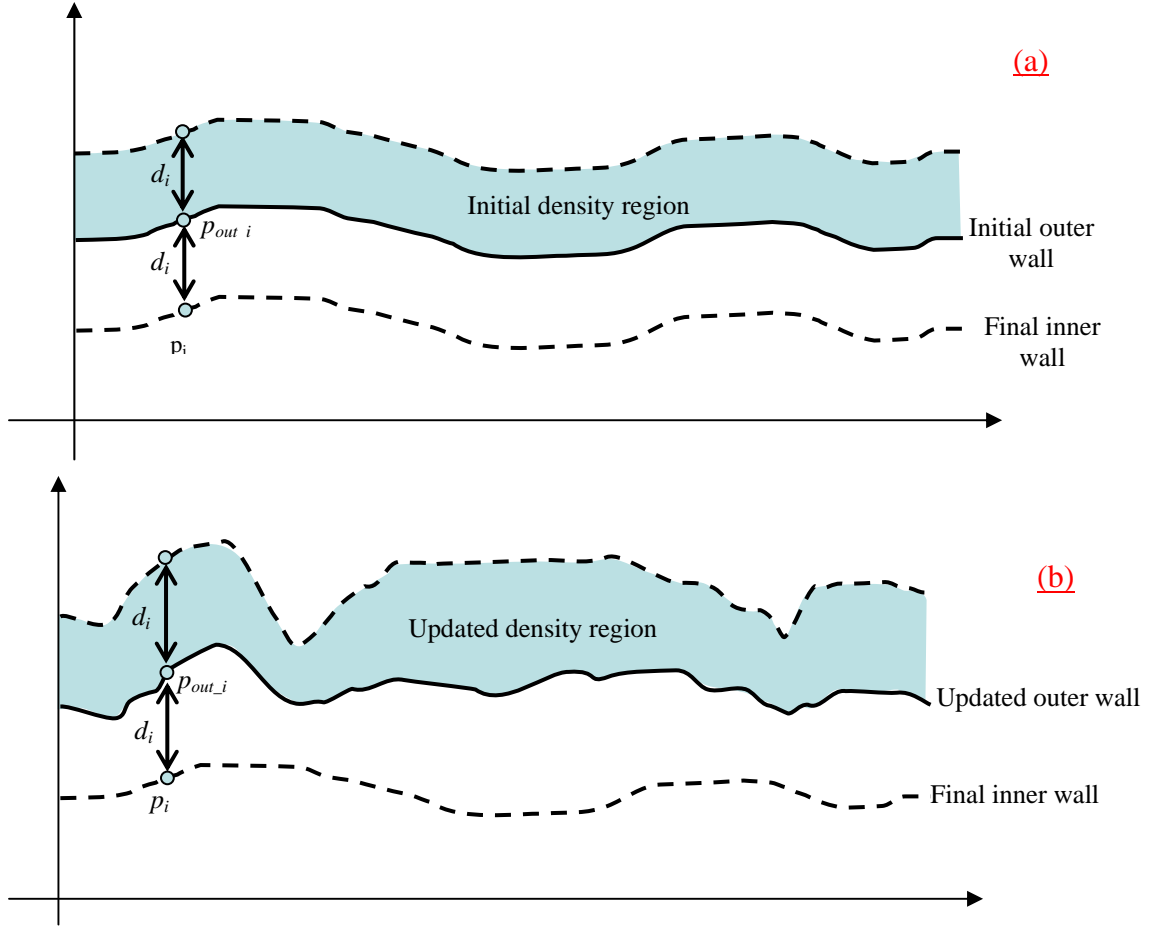


Figure 7: Local region-based process. The graph (a) represents the initial estimation of the outer wall from the final inner wall segmentation. The distance d_i between polygon points p_i and p_{out_i} is equal along the contour. In gray is the targeted region within d_i distance of the outer wall. On the graph (b), the outer wall evolves as the distance between p_i and p_{out_i} does. Region based segmentation is done using the targeted density region in white between the outer and inner walls estimation.

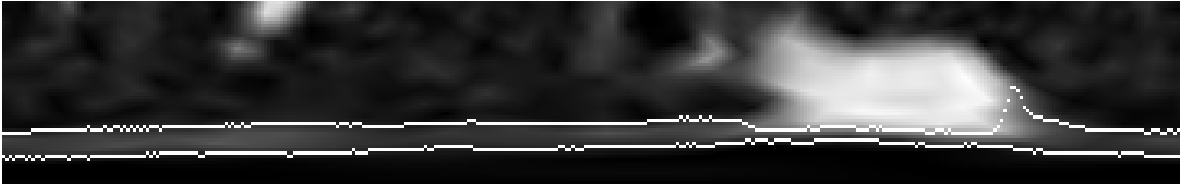


Figure 8: Iteration 999: The wall is well defined and stable using the local region-based segmentation, but around the artery it is both under and over segmented.

When an artery touches an airway boundary, it becomes difficult to evaluate the wall at this particular location. It is next-to-impossible to differentiate the artery and airway borders. A possible solution is to extrapolate the airway boundary using an approximation of the wall thickness elsewhere. We integrate this solution into a parameter of our speed function.

The distance parameter in our speed term can be expressed as follows:

$$dist = (d_i - \bar{d}) \cdot H(I(p_{out_i}) - k \cdot \mu_{wall}) \quad (14)$$

Where d_i is the distance at p_{out_i} , \bar{d} is the mean distance across the whole contour, H represents the Heaviside function $H(x)$, k a fixed parameter and μ_{wall} the average intensity of the wall. The idea is to use this distance term only when the polygon point is within the neighborhood of an artery, meaning a high density neighborhood. Therefore, the density value at p_{out_i} is checked against the mean intensity value of the whole wall, between inner and outer estimation. A weight is assigned to the mean to ensure the high density parameter of the artery is met.

The complete speed term is then the following:

$$\frac{\partial r}{\partial t} = \begin{pmatrix} \lambda_1 (I(p_{out_i}) - v_{in}(d_i))^2 - \lambda_2 (I(p_{out_i}) - v_{out}(d_i))^2 + \alpha \cdot K \\ -(d_i - \bar{d}) \cdot H(I(p_{out_i}) - k \cdot \mu_{wall}) \end{pmatrix} \cdot N \bullet \begin{bmatrix} 0 \\ 1 \end{bmatrix} \quad (15)$$

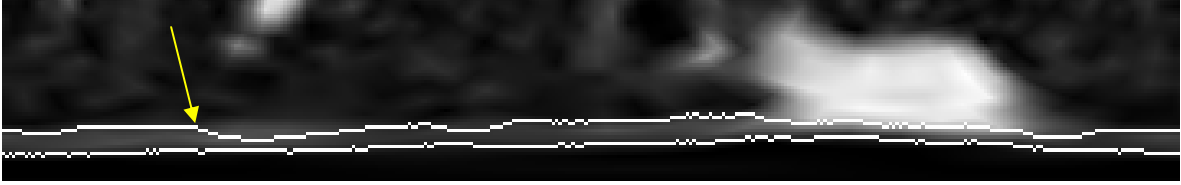


Figure 9 Outer wall evolution, iteration 100. Local region based segmentation forces an under-segmentation (arrow) in case of uniformity within the wall. Curvature constraint helps smooth out the final curve

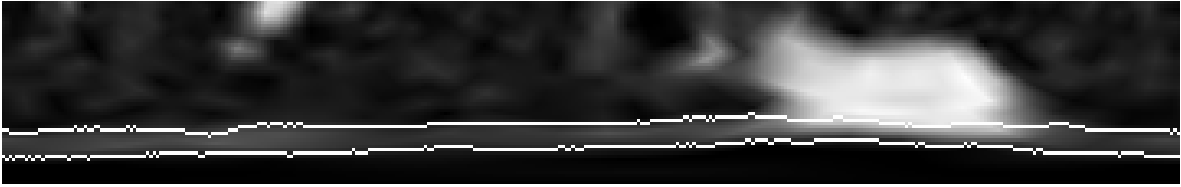


Figure 10 Outer wall evolution, iteration 269. Curvature constraint helps smooth out the curve

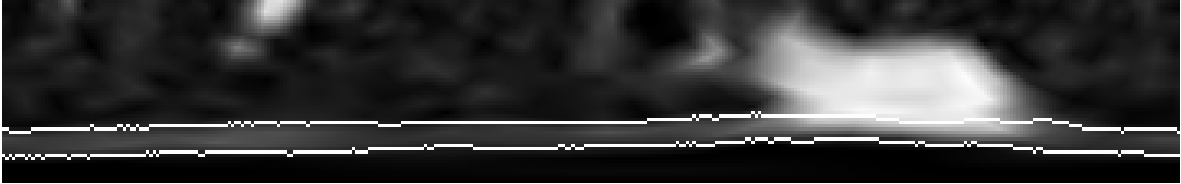


Figure 11. Outer wall evolution at iteration 525. Curvature has smoothed out the curve. The distance speed brings up the contour inside the artery region for extrapolation.

3. MATERIALS AND RESULTS

3.1. Materials

We performed two sets of tests to evaluate our approach. First, we applied our segmentation approach on phantom datasets that consist of PVC tubes of known dimensions, scanned perpendicular to the tube axes at a voxel resolution of $0.35 \times 0.35 \times 0.5 \text{ mm}^3$. The inner diameters varied between 2mm and 10mm; the wall thicknesses between 1mm and 3mm. The use of phantom datasets help validate the sub-voxel accuracy provided by the active contour approach.

Secondly, we also tested the active contour algorithm on human datasets. Thirty-five sub-segmental bronchi from a patient clinically diagnosed with moderate to severe bronchiectasis were randomly selected. Most of locations included an accompanying artery so the robustness of the algorithm in such situations could also be tested. The patient was scanned at a voxel resolution of $0.58 \times 0.58 \times 0.79 \text{ mm}^3$. Two independent readers at two different time periods

manually measured the airway inner and outer diameters using electronic calipers. These inter- and intra-observer measurements were then compared to those of the active contour algorithm.

3.2. Results

On phantom data, the active contour approach shows sub-voxel accuracy with an average error of 0.108mm for the inner diameter and 0.141mm for the outer diameter. Results, reported in Figure12 and Table 1, show that the largest variations occur for the 2 largest tubes in the evaluation of inner diameter and in the 3 smaller tubes for the outer diameters, although the segmentation still achieves sub-voxel accuracy in all cases.

On real datasets, the average variation between the manual measurements and the active contour is 0.14mm and 0.18mm for inner and outer diameters respectively. Results are reported in Figure 13. The red circles which correspond to the error of the automated method for a specific airway, are located within the operators' errors for both inner and outer diameters.

The average processing time to compute airway boundaries is about 1 second or less on average.

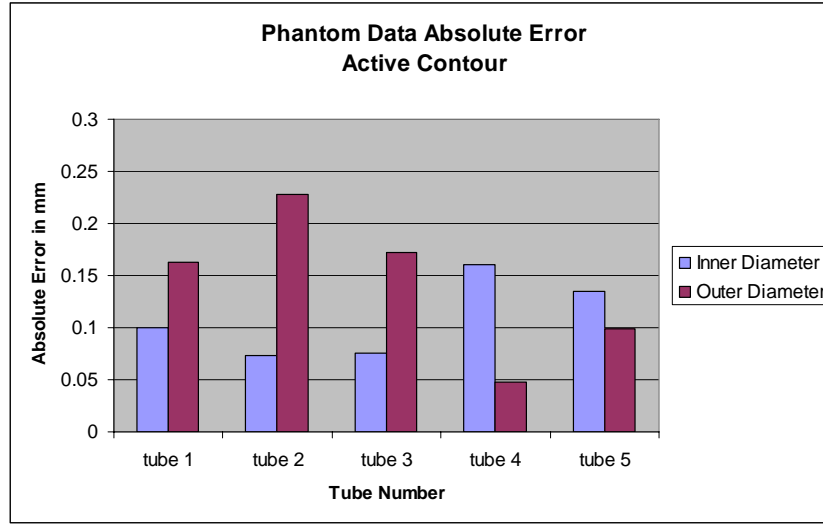


Figure 12: Absolute error in mm on Phantom Tubes for the Active Contour approach. Sub voxel accuracy (voxel resolution – 0.29mm³) is reached for all the tubes.

Table 1: Evaluation results of Active Contour measurements on phantom data. For each tube, the average diameters as well as standard deviation of the 5 measurements are reported for both inner and outer diameters.

Active Contour	Inner Diameter		Outer Diameter	
	Average (mm)	Standard Deviation (mm)	Average (mm)	Standard Deviation (mm)
Tube 1	1.879	0.01	4.439	0.026
Tube 2	3.176	0.073	6.351	0.066
Tube 3	6.316	0.075	9.751	0.077
Tube 4	6.637	0.159	12.58	0.041
Tube 5	9.380	0.135	15.56	0.098

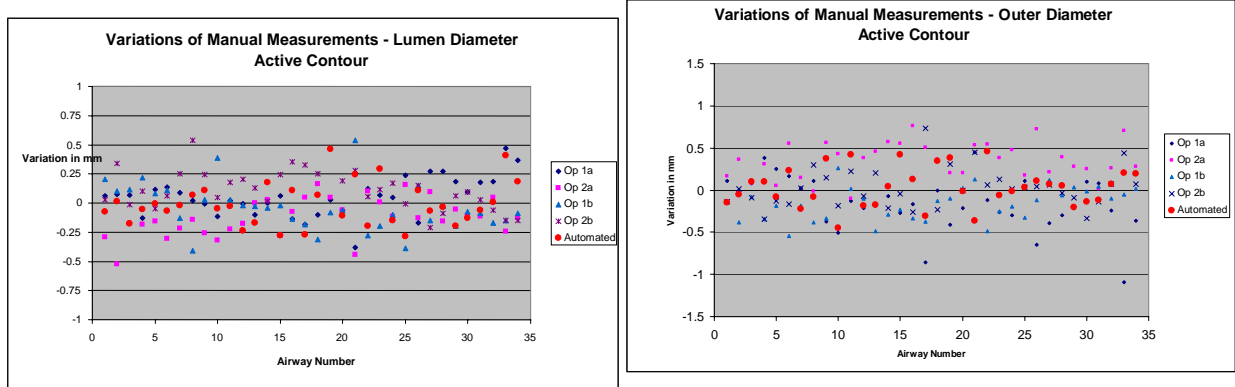


Figure 13: Variation of manual measurement with active contour for inner (left) and outer (right) diameters. Each symbol represents the difference between the automated or manual measurement with the average value. Op1a indicates measurements made by operator 1 at time 1, Op2a is operator 2 at time 1, Op1b is operator 1 at time 2, and Op2b is operator 2 at time 2. Shown in red circles, automated measurements are located well within the human error margin for both cases.

4. CONCLUSION

We have presented a novel method to measure airway dimensions. This method is based on region intensity separation using active contour techniques. No manual initialization is required; the system uses instead the automatically computed tracheobronchial centerline points to set an initial contour. Segmentation of the lumen boundaries uses the technique proposed by Chan *et al* with region-based active contour [10]. The computation of outer boundaries takes into account a local region differentiation as well as the average intensity of the wall to detect and exclude accompanying arteries.

Preliminary results demonstrate sub-voxel accuracy on phantom datasets and an average error on human datasets of 0.14mm and 0.18mm for inner and outer diameters respectively.

Comparison with the Full Width Half Maximum (FWHM) approach, as shown in Figure 14, reveals an advantage in the determination of airway boundaries, specifically in cases with nearby arteries. On the left, the FWHM method steps inside the artery for the outer diameter and we can also notice an over-segmentation of the inner boundary around the vessel region. On the right, the vessels are nicely excluded from the airway segmentation using the active contour approach; no over-segmentation is noticed for inner boundary.

Although this approach is used for measurements at specific selected locations on bronchi, one can imagine that an active plan could be utilized to fit the whole bronchus and then help detecting / monitoring local abnormalities such as local lumen dilatation or bronchial stenosis.

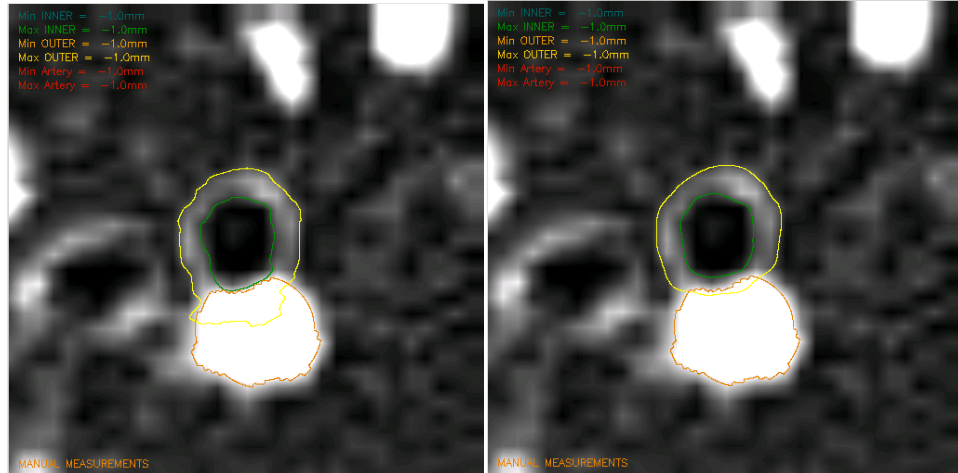


Figure 14: A comparison of airway measurement methods. The outer diameter is indicated by yellow and the inner diameter by green. On the left, measurement by FWHM method shows over-estimation of the outer airway boundary where it is adjacent to the artery, because the maximum value that is used to compute the airway contour is affected by the artery. On the right, the method using the active contour excludes the artery from the outer airway segmentation.

Although more exhaustive tests are needed for better validation, the method already shows accurate measurements of airway dimensions for both inner and outer diameters, which is critical for the detection and monitoring of structural changes and consequently for the evaluation of the severity and extent of bronchial pathologies.

REFERENCES

1. Amirav I., Krammer S. S., Grunstein M.M., and Hoffman E.A. "Assessment of methacholine-induced airway constriction by high-resolution cine computed tomography (HRCCT)" J. Applied Phys., 75(5):2239-2250, 1993
2. Kiraly A.P., Reinhardt J.M., Hoffman E.A., McLennan G., and Higgins W.E., "Virtual Bronchoscopy for Quantitative Airway Analysis", SPIE Medical Imaging 2004, Physiology, Function, and Structure from Medical Images, Vol. 5746, p369-383
3. Wiemker R., Blaffert T., Bulow T., Renisch S. and Lorenz C. (2004): "Automated assessment of bronchial lumen, wall thickness and bronchioarterial diameter ratio of the tracheobronchial tree using high-resolution CT" Computer Assisted Radiology and Surgery 2004, International Congress Series 1268 967-972.
4. Saba O.I., Hoffman E.A., Reinhardt J.M., "Maximizing quantitative accuracy of lung airway lumen and wall measures obtained from X-ray CT imaging", J. Appl Physiol 95:1063-1075
5. Prêteux F, Fetita C., Grenier P. "Modeling, segmentation, and caliber estimation of bronchi in high-resolution computerized tomography" Proceedings SPIE Conference on Statistical and Stochastic Methods in Image Processing II, San Diego, CA, Vol. 3167, July 1997, p. 58-69.
6. Prêteux F., Fetita C.I., Capderou A., Grenier P., "Modeling, segmentation and caliber estimation of bronchi in high resolution computerized tomography", Journal of Electronic Imaging 1999, Vol. 8, Issue 1, p36-45
7. Tschirren J, Hoffman EA, McLennan G, and Sonka M, "Intrathoracic Airway Trees: Segmentation and Airway Morphology Analysis From Low-Dose CT Scans," IEEE Trans. Medical Imaging December 2005, Vol 24, No.12
8. A P Kiraly, B L Odry, D P Naidich, C L Novak, "Boundary-Specific Cost Functions for Quantitative Airway Analysis," MICCAI 2007.
9. Casselles V., Kimmel R., Sapiro G., "Geodesic Active Contours", International Journal of Computer Vision 1997, Vol 22, p61-79
10. Chan T.F., Vese L.A., "Active Contours without Edges", IEEE Transactions on Image Processing 2007, Vol. 10, No 2, p266-277
11. Kiraly A.P., McLennan G., Hoffman E.A., Reinhardt J.M., and Higgins W.E., "Three-dimensional human airway segmentation methods for clinical virtual bronchoscopy." Academic Radiology, 2002. 9(10): p. 1153-1168.
12. Kiraly A.P., Helferty J.P., Hoffman E.A., McLennan G. and Higgins W.E. "Three dimensional path planning for virtual bronchoscopy" in IEEE Transactions on Medical Imaging. vol. 23, no.1, November 2004:p.1365-1379
13. Odry B.L., Kiraly A.P., Novak C.L., Naidich D.P., Lerallut J-F (2005) "A visualization tool for global evaluation of bronchiectasis and local evaluation of the airways" European Medical & biological Engineering conference EMBEC'05 Proceedings; Prague, November 2005
14. Grenier P.A., Beigelman-Aubry, C. Fetita, Preteux F., "New Frontiers in CT imaging of airway diseases", European Radiology, Vol. 12, pp1022-1044